High-Performance Chip Design With Parallel Architecture for Magnetic Field Imaging System

Ming-Yi Lin, Sheng-Hsien Hsieh, Ching-Han Chen, and Chun-Hung Lin

***Abstract*— To address the limitations of typical coil detection systems and enhance the performance of traditional magnetic field imaging (MFI) systems, we propose a MFI system that uses a 4 × 4 array of anisotropic magnetoresistance (AMR) sensors. The core controller of the proposed system was designed using a pipelined parallelization algorithm and implemented on a high-speed field-programmable gate array (FPGA) in a fully hardware-based architecture. The designed MFI system can achieve parallel acquisition of magnetic field components from the 16-channel AMR sensor array, parallel data processing, parallel data transmission, and parallel computations in a single cycle of only 4 ms. Compared with typical detection systems, the proposed solution not only exhibits superior performance but can also provide dynamic visual representations of sensed information.**

***Index Terms*— Magnetic field imaging (MFI), magnetic field sensor array, nondestructive testing (NDT), parallel architecture and algorithm.**

I. Introduction

A. Background

NONDESTRUCTIVE testing (NDT) technologies are intended to reveal defects in parts, systems, or materials by identifying discontinuities or differences in characteristics without damaging the target. NDT methods have been widely applied to inspect and characterize composite defects in materials and composites in industries and applications such as transportation, power plants, aviation, nuclear energy, construction, pressure vessels, and storage tanks.

In many nondestructive evaluation methods, the inspected material is excited through electromagnetic induction and the resulting magnetic flux density or magnetic intensity is then measured. Eddy current testing (ECT) and magnetic flux leakage (MFL) are the most commonly used electromagnetic-induction-based NDT methods. ECT and MFL can be applied to structures with simple shapes, such as flat plates or cylinders. They can also be used to detect subsurface defects in coatings. Methods of inspecting defects in materials using ECT and MFL technologies have been extensively investigated [1], [2], [3], [4], [5], [6], [7], [8], [9], [10], [11], [12], [13], [14], [15], [16], [17].

In [1], a novel flexible sensor array comprising 16 differential coils was developed as an ECT probe for inspecting curved surfaces. Simulated experiments were performed with MATLAB, and a 3-D finite-element method (FEM) model was employed for simulated inspections of stainless-steel plate samples and curved turbine blade samples. The experimental results revealed that the probe could detect eight types of artificial defects in stainless steel plates and 15 types of artificial defects in curved turbine blades.

In [2], another prototype flexible-array ECT probe was developed that contained 16 tunneling magnetoresistance (TMR) sensors. The probe was employed to inspect 3-D curved structures. The excitation frequency was studied using a 3-D finite-element numerical model in MATLAB, and the probe was optimized for the detection of buried defects. The experimental results demonstrated that the probe could accurately detect 16 types of artificial defects on the inner walls of two cylindrical samples.

A flexible-array ECT probe was designed with differential coil sensors in [3]. The prototype probe contained a pair of coil sensors fabricated on a flexible printed circuit board (PCB) and was applied to inspect curved carbon-fiber-reinforced polymer (CFRP) structures. This flexible probe operated on the principle of electromagnetic induction and could be used as an ECT inspection tool. FEM modeling was used to observe the electromagnetic induction characteristics of curved CFRP structures, enabling the detection of samples with anisotropy or low conductivity. Further analysis and optimization of the probe were performed using a 3-D FEM model. The experimental results demonstrated that the probe could identify small defects measuring 2 mm in length, 1 mm in width, and 0.4 mm in depth on the curved surfaces of the CFRP samples.

A prototype ECT array probe with 64 TMR sensors that were microfabricated and packaged on the probe was developed and tested in [4]. In the prototype probe, the distance between any two adjacent TMR sensors was 0.5 mm. Through analysis of the magnetic field imaging (MFI) output, defects

Manuscript received 16 August 2023; revised 20 October 2023; accepted 1 November 2023. Date of publication 17 November 2023; date of current version 29 December 2023. This work was supported in part by the National Science and Technology Council, Taiwan, under Grant NSTC 112-2222-E-155-003-MY2; and in part by the Special Fund of Yuan Ze University. The Associate Editor coordinating the review process was Dr. Alvaro Hernandez. *(Corresponding author: Ming-Yi Lin.)*

Ming-Yi Lin is with the Department of Computer Science and Engineering, Yuan Ze University, Taoyuan 320315, Taiwan (e-mail: pk4881@gmail.com; lmy@saturn.yzu.edu.tw).

Sheng-Hsien Hsieh is with the Program of Artificial Intelligence and Mechatronics, National Pingtung University of Science and Technology, Pingtung 912301, Taiwan (e-mail: georgeh@npust.edu.tw).

Ching-Han Chen is with the Department of Computer Science and Information Engineering, National Central University, Taoyuan 32001, Taiwan (e-mail: pierre@g.ncu.edu.tw).

Chun-Hung Lin is with International Games System Company Ltd., New Taipei City 248, Taiwan (e-mail: jiunhung1982@gmail.com).

Digital Object Identifier 10.1109/TIM.2023.3334351

1557-9662 © 2023 IEEE. Personal use is permitted, but republication/redistribution requires IEEE permission.
See https://www.ieee.org/publications/rights/index.html for more information.

Authorized licensed use limited to: National Central University. Downloaded on July 02,2024 at 07:18:47 UTC from IEEE Xplore. Restrictions apply.

could be identified and located. The experimental results indicated that the prototype probe was highly sensitive to horizontal and vertical defects and could identify small defects measuring 1 mm in length, 0.2 mm in width, and 1 mm in depth with the aid of an artificial neural network.

In [5], a prototype ECT array probe comprising 64 TMR sensors packaged on a PCB was designed. The array ECT probe was employed to inspect aluminum plates and rivet fixations for assessing fastener tilt. To ensure that the measurements were accurate and prevent errors due to manual operation, an optical method was employed to precisely measure the fastener tilt. MFI was simulated using the commercial FEM software COMSOL Multiphysics. The measured results demonstrated that the array ECT probe could distinguish tilted from untilted fasteners when the tilt altitude was at least 0.18 mm.

A high-density prototype ECT array probe comprising 180 TMR sensors was developed in [6] to perform MFI inspections of multilayer riveted aluminum structures. The spacing between the TMR sensors was 0.5 mm, and the width of the scanning area for each scan was 90 mm. The results indicated that the probe could detect microdefects of size $300 \times 300 \times 400$ μm on multilayer aluminum samples.

Implementing the aforementioned array ECT probe systems requires the typical design of additional circuits, such as those for coil systems, amplification, filtering, and excitation frequency adjustment; moreover, complex equipment and instruments—including a PC as a central controller, a generator for creating excitation signals, and a data acquisition (DAQ) system—are also necessary for defect detection.

MFL testing [8], [9], [10], [11] is a widely used NDT method for detecting corrosion, material loss, and pitting in steel structures. The basic principle of the MFL method is the magnetization of the ferromagnetic metal object to near saturation with a powerful magnetic field. The magnetizer for this task can be either a magnet or a magnetizing coil. If the object has no flaws, the magnetic flux is not disturbed.

The magnetic flux is constrained in ferromagnetic materials because of their high permeability; however, if a defect exists, the magnetic field leaks from the material into the nearby air, producing a leakage field.

Hayashi et al. [8] proposed an inspection method in which unsaturated ac MFL (USAC-MFL) is used for identifying defects in the steel bars of reinforced concrete and avoiding the influence of the concrete itself. The USAC-MFL sensor array probe contains six combined anisotropic magnetoresistance (AMR) magnetic sensors. The USAC-MFL uses a weak ac magnetic field based on the MFL method for determining the initial magnetization characteristics of steel. This magnetic sensor array is also useful for obtaining the phase of the magnetic field, which can clarify the obtained data and facilitate the identification of a fracture.

Hayashi et al. [9] developed a sensor array probe using USAC-MFL for detecting cracks in the weld shapes of steel structures. Experiments were performed for both cracked and uncracked areas, and the obtained MFL signals were analyzed.

B. Motivation

We surveyed many state-of-the-art technologies related to magnetic NDT methods, including ECT and MFL. Although ECT and MFL are popular NDT technologies, they have some disadvantages; specifically, they may have insufficient accuracy or robustness, require additional hardware, or are expensive.

ECT and MFL are applicable for structures with simple shapes, such as cylinders and flat plates [8]. Using ECT and MFL methods to analyze other shapes or complex structures is challenging. Additionally, magnetic NDT inspection methods are affected by magnetic noise because ferromagnetic materials have nonuniform magnetic permeability [8]. If ECT and MFL are used to analyze steel structures, numerous magnetization signals are obtained; distinguishing the measured ECT and MFL signals from the defect signal is difficult because of differences in the magnetic signal intensity and the nonuniform magnetic permeability. Hayashi et al. [8] introduced a strong dc magnetic field to ensure magnetic saturation and minimize the effect of the nonuniform magnetic permeability. This method was, however, found to require a kilowatt-class electrical power supply.

The coil sensor used in these technologies is one of the simplest sensors that can measure a magnetic field; however, sensor array probes containing coils have limited sensitivity for detecting buried defects in structures. The coil sensor operates at a low frequency, and the depth of the eddy current (EC) flowing in a conductive material is inversely proportional to its excitation frequency. The induced signal is proportional to the rate of change of the flux; therefore, a low excitation frequency is necessary to detect defects buried in the material [2]. Additionally, ECT has a very low signal-to-noise ratio (SNR) [6]. The SNR is related to the square root of the product of the electrical conductivity of the material and the frequency of the excitation current [2]. This relationship also suggests that the excitation frequency must be low for a buried defect to be detected.

Some scholars, moreover, declared that conventional coil sensors can only detect whether a defect exists; they cannot precisely locate defects [17]. In [17], the accuracy of detection was affected by the large volume of the coil detection system and the coupling between coils.

In spite of the high sensitivity and linearity of state-of-the-art technologies when measuring a magnetic field, integrating a coil sensor (including excitation, induction, and pickup coils) into an electronic circuit is more challenging than integrating other sensors because these state-of-the-art sensors are manufactured through a microfabrication process. This process is inaccessible and inconvenient, resulting in high development times and costs and greatly reducing the commercial competitiveness of these state-of-the-art magnetic NDT technologies. The development process is not only expensive in terms of person-hours but also leads to longer product delivery times to the market. In summary, the research, development, and time costs for coil sensors are higher than those for other sensors.

Adopting the FEM for investigating NDT methods with these state-of-the-art technologies can be, moreover,

Authorized licensed use limited to: National Central University. Downloaded on July 02,2024 at 07:18:47 UTC from IEEE Xplore. Restrictions apply.

time-consuming, costly, or risky. In [12], a magnetic-EC measurement system based on an AMR sensor was proposed, and a distributed current source (DCS) method through which the magnetic flux density generated by ECs in a nonmagnetic metal conductor can be calculated directly was introduced. The DCS method improved the accuracy and efficiency of estimations and outperformed the FEM for measuring generated magnetic fields. That study also indicated that the FEM may have large errors [12]; however, the MFI for these technologies is typically simulated using FEM with a commercial software solution.

In spite of their high accuracy, the state-of-the-art technologies are usually implemented using digital signal processing (DSP) or custom application-specific integrated circuits (ASICs). Achieving sufficient performance with DSP or an ASIC requires the design of additional circuits, such as those for analog-to-digital converters, and instruments, such as a function generator, bidirectional dc power supply, or DAQ system.

NDT technologies have been developed with the goals of rapidly, reliably, and cost-effectively inspecting defects. The novel magnetic NDT technologies, however, have numerous disadvantages and are expensive, hindering the further development of electromagnetic NDT and preventing their extensive use in real scenarios.

Recently, magnetoresistive (MR) sensors based on microelectromechanical systems (MEMSs) have been improving in terms of speed, sensitivity, resolution, and affordability. Numerous studies—such as [12], [13], [14], [15], and [16]—have noted other advantages of MR sensors, such as their small package size, lightness, and placement flexibility.

As described in [12], AMR sensors have better sensitivity and linearity for measuring the state of a magnetic field than do coil sensor systems.

Huang and Jeng [13] proposed an MFI system that has an array scanning configuration of 16 AMR sensors arranged in a single row. This 16-channel AMR sensor array architecture includes a microcontroller unit (MCU) for control and data transmission. The system was employed to scan PCBs to produce visualizations of magnetic field maps from the 2-D current density distribution, which was calculated with a 2-D Fourier transform algorithm. During the scanning process, the object was placed on a xy translation stage; each scan required 20 s and covered a scanning range of 90 $\times$ 100 mm. The system could determine the 2-D current distribution for the magnetic field maps of printed circuits with a minimum spacing of 2 mm.

Rahmawati et al. [14] and Suksmono et al. [15] proposed an MFI system based on 16 AMR sensors (HMC5883L) arranged in a 4 $\times$ 4 grid and with a spacing of 6 cm. In a previous study, the authors had constructed a magnetic imaging system using the built-in magnetometer of a smartphone. The MFI system used a 16-channel multiplexer (MUX4067) to connect the 16 AMR sensors. The system scanned areas of interest and obtained the x-, y-, and z-axis components of the magnetic field. An MCU sequentially controlling the multiplexer received and stored magnetic field data from the 16 AMR sensors in a data buffer through an interintegrated circuit (I^2C) bus. A bicubic interpolation technique was then used to construct magnetic field images of the magnetic objects. Notably, the system could detect changes in position as it approached or moved away from a magnetic object.

Investigating and surveying the state-of-the-art technologies for magnetic NDT revealed some challenges and recommendations for future development.

1) The hardware resources of MCUs are limited, and their performance is inadequate to meet the I/O communication demands of the sensor array. These systems also usually require a DAQ system to capture magnetic field signals or multiplexers for multichannel data fusion. This hardware stack leads to data transmission delays and affects the precision of magnetic field acquisition.
2) Laboratory circuit designs for electromagnetic detection systems and based on ECT and MFL methods are usually complex, and these systems require support from other equipment, instruments, and devices. These systems are inflexible and impractical; moreover, maintaining them is challenging.
3) MFI is often simulated using commercial software such as Ansys Maxwell, COMSOL Multiphysics, and MATLAB. Building MFI software with such commercial packages incurs additional costs, and these software solutions may need to be regularly updated to remain compatible with an operating system. Consequently, these systems are constrained by commercial software and lack flexibility and usability.
4) Employing industry-related commercial NDT equipment, such as high-performance ECT solutions, has a high unit cost; such methods are expensive to implement in industrial setups.

In this article, we propose an efficient parallel computing system framework, a high-speed field-programmable gate array (FPGA)-based parallel controller, and a 4 $\times$ 4 AMR sensor array for magnetic field sensing for NDT in MFI applications.

The design of the MFI system in this study addresses various problems and provides contributions as follows.

1) The system uses an FPGA parallel controller to accomplish parallel computation for multiple functional modules, addressing the problem of insufficient MCU performance and achieving high-level system integration.
2) The parallel controller does not have the hardware resources and peripheral I/O limitations that MCUs do, enabling high-speed communication and parallel transmission for multiple sensor arrays.
3) The system overcomes the drawbacks of typical coil detection systems in terms of flexibility, practicality, and maintenance and is thus more practical.
4) By using an AMR sensor array to construct an MFI system, the design time and development cost are lower than that for complex coil detection systems; moreover, the system's stability, reliability, and real-time capabilities are superior.

Authorized licensed use limited to: National Central University. Downloaded on July 02,2024 at 07:18:47 UTC from IEEE Xplore. Restrictions apply.

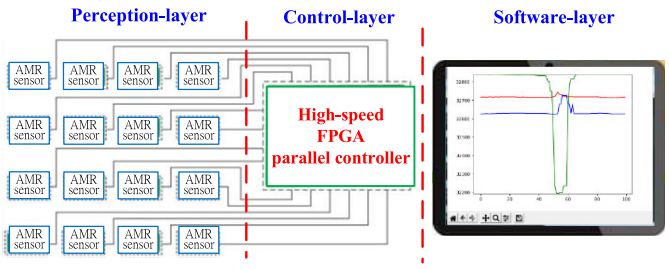


Fig. 1. Overall architecture of the MFI system.

5) The system does not require additional laboratory equipment support; instead, data stacking is performed at the hardware layer, reducing transmission delays.
6) The developed dynamic visualization imaging software reduces the need for commercial software, which is expensive and has various limitations. This software enhances the system's usability.

C. Structure of This Article

The sections of this article are organized as follows: Section II presents the overall architecture of the MFI system, including the hierarchical modular design of key functional modules. In Section III, the behavioral modeling, working principles, and high-level hardware synthesis of the pipelined parallel controller are briefly described. Section IV discusses the implementation, system validation, and performance evaluation of the MFI system. Finally, Section V provides a summary of the conclusions of this study.

II. Overall Architecture of MFI System

In this article, we propose an MFI system based on multiple AMR sensors that form a sensor array. The system was designed with a parallel computing architecture and the goals of integrating management of the underlying magnetic field sensor array, achieving magnetic field DSP, and integrating with MFI software. As shown in Fig. 1, the MFI system has three layers: the perception layer, the control layer, and the software layer.

The perception layer comprises 16 AMR sensors based on MEMS technology, with these sensors forming a 4×4 array. This sensor array platform is responsible for synchronously reading the subtle magnetic field variation components of the detected targets. We adopted MEMS fabrication for the perception layer to ensure a lower processing time than that of coil detection systems and prevent unnecessary electromagnetic interference.

The control layer's high-speed FPGA parallel controller serves as the core of the entire MFI system. It is responsible for DSP, sensor array control and management, and feature data transmission and communication with the software system.

The software layer of the system's imaging software is primarily responsible for real-time visualization of the dynamically detected information. The system's imaging software facilitates real-time collaborative operation and high-speed synchronous feature data transmission between the high-speed parallel controller and the sensor array platform.

The most critical component of the proposed system is the parallel controller in the control layer. The parallel controller's functions include managing the 16 AMR sensors in the sensing layer, parallel acquisition of sensor data, parallel computing of data, and connecting to the imaging software in the software layer for real-time dynamic visualization. In the design and integration of the parallel controller, various intelligent computing architectures and unique DSP functionalities were embedded in each module; each functional module was designed to have unique communication interfaces and interfacing protocols. The modules are interactive, interoperable, interconnected, and intercommunicative. The design and integration processes involve various challenges; therefore, an effective and efficient design methodology was necessary.

A. Hierarchical Design and Hardware Synthesis Methodology

In this study, we adopted an effective and efficient systematic design methodology to design and integrate the real-time complex parallel controller system.

This section briefly explains hierarchical design and synthesis methodology for complex systems; this methodology facilitates the effective implementation and rapid prototyping of an embedded real-time system.

First, hierarchical modular formalization was performed by decomposing the complex parallel controller system into independent modules; each module was considered a discrete-event system (DES). Next, we employed a set of synthesis rules [20] to rapidly generate hardware circuits for each DES model, including the interfacing protocol between modules. Finally, each DES model was synthesized into a large-scale integration (VLSI) hardware circuit by using hardware description language (HDL).

For detailed steps and information regarding the methodology of hierarchical modular design, discrete-event modeling, HDL synthesis rules, and hardware synthesis, please refer to the literature [18], [19], [20], [21], [22], [23], [24], [25], [26], and [27].

B. Hierarchical Modular Design of the Parallel Controller

Fig. 2 presents the hierarchical modular architecture diagram of the parallel controller function module using IDEF0. This architecture is based on the functional hierarchy of automation and control systems. As shown in Fig. 2, the FPGA parallel controller (A0) module in the top layer is responsible for controlling the parameter settings governing communication and control between the four modules of the second layer. The four key controller modules of the main parallel controller are the magnetic sensor array controller (A1) module, the DSP function controller (A2) module, the software bridge controller (A3) module, and the functional unit (A4) module.

The magnetic sensor array controller (A1) module is responsible for controlling and monitoring the bottom-perception-layer AMR sensor array. The DSP function controller (A2) module is the core of the FPGA parallel controller. The A2 module is responsible for signal preprocessing, multichannel

Authorized licensed use limited to: National Central University. Downloaded on July 02,2024 at 07:18:47 UTC from IEEE Xplore. Restrictions apply.

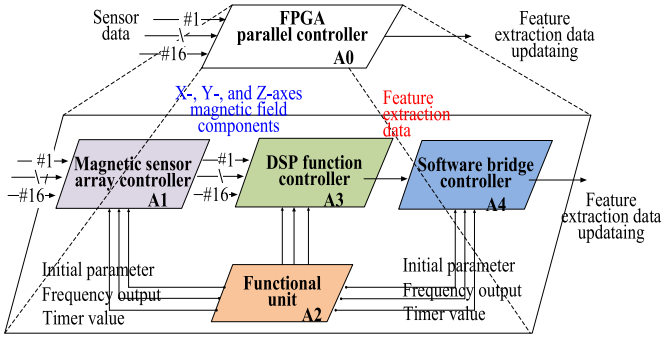


Fig. 2. FPGA parallel controller by IDEF0.

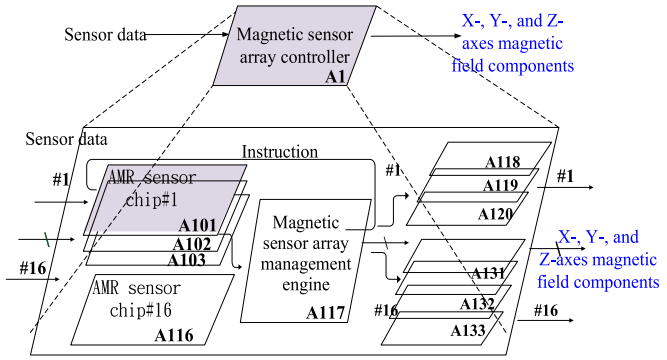


Fig. 3. Design of the magnetic sensor array controller.

data fusion, feature extraction, and implementing a defect detection model. The A2 module also controls communications among the other modules. Critically, the DSP function controller can overcome both hardware resource and synchronous delay problems because of the parallel algorithm design of the FPGA. Once the AMR sensor array data packets have been processed by the DSP module, the software bridge controller (A3) module receives the feature extraction data at the same time that the results of feature extraction are output to the imaging software.

The functional unit (A4) module is the function assistance module. The A4 module can implement the system initialization settings, calibrate parameters, and ensure that the system pipeline is operating correctly and effectively.

C. Magnetic Sensor Array Controller

The magnetic sensor array controller (A1) module controls and manages the AMR sensors at the bottom perception layer. As shown in Fig. 3, the A1 module is integrated with a magnetic sensor array management engine (A117), 16 AMR sensor chips (A101–A116), and 16 interintegrated circuits (I^2C) controllers (A118–A133). We designed a magnetic sensor array management engine based on primary/secondary architecture for the A1 module. The primary responsibility of the management engine is to drive the 16 child AMR sensors and issue control and read commands.

The 16 child AMR sensors perform synchronous measurements of the raw magnetic field components in the x-, y-, and z-directions. The parent engine, moreover, requests transmission of the microvariations in the received magnetic field components; the system then reads these data through its I^2C transmission interface. The design of the magnetic sensor array controller module is presented in Fig. 3.

D. DSP Function Controller

The DSP function controller (A2) module uses the Kalman filter for signal preprocessing, multichannel data fusion, and feature extraction. The process involves the following steps and equations.

1) Sensor Signal Preprocessing: For each sensor channel i, state prediction is performed

$$\hat{x}_{i,k|k-1} = F_{i,k}\hat{x}_{i,k-1|k-1} + B_{i,k}u_{i,k}$$

where $\hat{x}$ is the state vector estimate.

$\hat{x}_{k|k-1}$ is the predicted state estimate at time step k given measurements up to time step $k-1$.

$\hat{x}_{k|k}$ is the updated state estimate at time step k.

F_k is the state transition matrix that relates the state at time $k-1$ to the state at time k.

B_k is the control input matrix, which relates the control input u_k to the current state; u_k is the control input vector and represents the influence of external control on the state.

For each sensor channel i, error covariance prediction is performed

$$P_{i,k|k-1} = F_{i,k}P_{i,k-1|k-1}F_{i,k}^T + Q_{i,k}.$$

For each sensor channel i, the Kalman gain is computed.

$P_{k|k-1}$ is the predicted error covariance matrix at time step k given measurements up to time step $k-1$.

Q_k is the Kalman gain, which determines the weight given to the predicted and measured values in the state update

$$K_{i,k} = P_{i,k|k-1}H_{i,k}^T\left(H_{i,k}P_{i,k|k-1}H_{i,k}^T + R_{i,k}\right)^{-1}.$$

H_k is the measurement matrix that relates the state to the measurements.

R_k is the measurement noise covariance matrix and represents the uncertainty in the sensor measurements.

For each sensor channel i, the state estimate is updated

$$\hat{x}_{i,k|k} = \hat{x}_{i,k|k-1} + K_{i,k}\left(z_{i,k} - H_{i,k}\hat{x}_{i,k|k-1}\right)$$

z_k is the measurement vector at time step k.

For each sensor channel i, the error covariance is updated

$$P_{i,k|k} = \left(I - K_{i,k}H_{i,k}\right)P_{i,k|k-1}.$$

2) Multichannel Data Fusion: The combined state estimate and combined error covariance are as follows:

$$\hat{x}_{\text{combined},k|k} = \sum_{i=1}^{N} w_i\hat{x}_{i,k|k}$$

$$P_{\text{combined},k|k} = \sum_{i=1}^{N} w_i^2 P_{i,k|k}$$

where N is the number of sensor channels, and w_i is the weight assigned to each channel's state estimate.

Authorized licensed use limited to: National Central University. Downloaded on July 02,2024 at 07:18:47 UTC from IEEE Xplore. Restrictions apply.

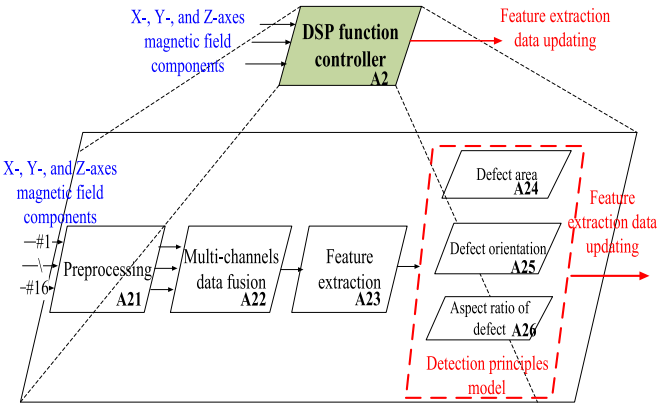


Fig. 4. Modeling design of the DSP function controller.

3) Feature Extraction: Relevant features are extracted from the combined state estimate $\hat{x}_{\text{combined}}, k|k$ to characterize essential information about the system.

The DSP function controller mainly operates in three steps as described in the preceding text. In the array, each sensor channel is individually processed using the Kalman filter to reduce noise. The filtered data are then fused with appropriate weights to create a robust dataset for feature calculation. Finally, relevant features are extracted from the combined state estimate to generate the detection principles model.

As illustrated in Fig. 4, the DSP function controller was developed through a hierarchical modular design of its preprocessing (A21) submodule, data fusion (A22) submodule, feature extraction (A23) submodule, and the main detection principles model. The detection principles model calculates four feature values for each inspection block, namely the defect area (A24), defect orientation (A25), defect color depth (A26), and defect aspect ratio (A27). The design of the DSP function controller for magnetic signal processing is presented in Fig. 4.

E. Software Bridge Controller

The software bridge controller (A3) module plays a crucial role in maintaining precise communication between the main parallel controller and the software system. The A3 module is responsible for transmitting and receiving feature extraction data. It achieves this by using a high-speed serial peripheral interface (SPI) connection to transmit feature data. An SPI is a highly effective communication interface for monitoring the state of a system. The SPI offers numerous benefits, including a compact pin configuration, a simple structure, high transmission speed, and ease of use. As depicted in Fig. 5, the software bridge controller architecture includes the SPI receiver submodule (A31), the high-speed bridge controller submodule (A32), and the SPI transmission submodule (A33).

The SPI receiver submodule processes the received feature extraction data and transmits it to the high-speed universal asynchronous receiver/transmitter (UART) controller. UART controller module mainly controls the communication with the imaging software module and features data packaging and processing tasks. The feature extraction data residing in the data register are then transferred in real time to the imaging software through the SPI.

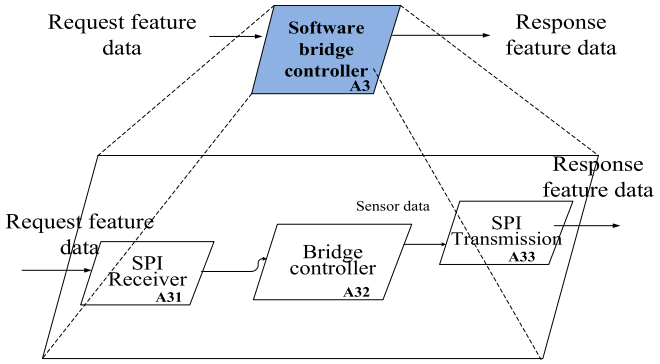


Fig. 5. Modeling design of the software bridge controller.

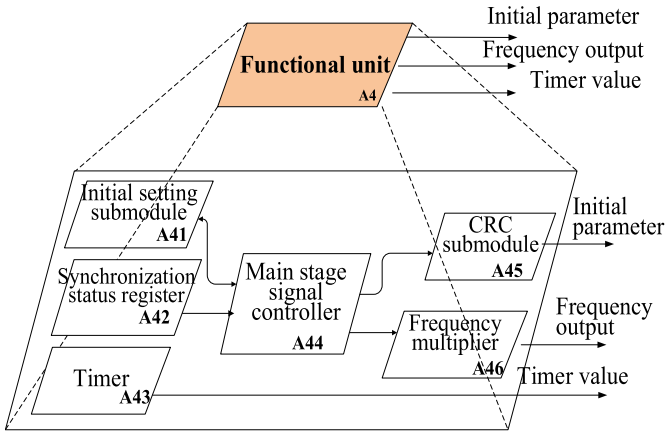


Fig. 6. Modeling design of the functional unit.

F. Functional Unit

The functional unit (A4) module is an essential component of the MFI system and is responsible for achieving precise time-synchronized DAQ between the main parallel controller and the 16 AMR magnetic resistance sensors.

The A4 module comprises six submodules: the initial setting submodule (A41), synchronization status register (A42), timer submodule (A43), main stage signal controller (A44), CRC submodule (A45), and frequency multiplier submodule (A46), as shown in Fig. 6.

The initial setting submodule provides the system initialization settings and calibrates the system parameters to ensure that the system operates effectively. The synchronization status register and timer submodules work together to achieve precision time synchronization between the main parallel controller and the magnetic field sensor array.

The main stage signal controller (A44) submodule is the core of the functional unit (A4) module. The pipelined stage controller plays a crucial role in efficiently controlling the parallel execution of all multicontroller module; therefore, we integrate the stage signal controller (A44) submodule into the functional unit (A4) module to act as the pipelined stage controller for the system.

The stage signal controller generates state transition control signals, enabling the successive activation of each task submodule. The functional unit is a function assistance module

Authorized licensed use limited to: National Central University. Downloaded on July 02,2024 at 07:18:47 UTC from IEEE Xplore. Restrictions apply.

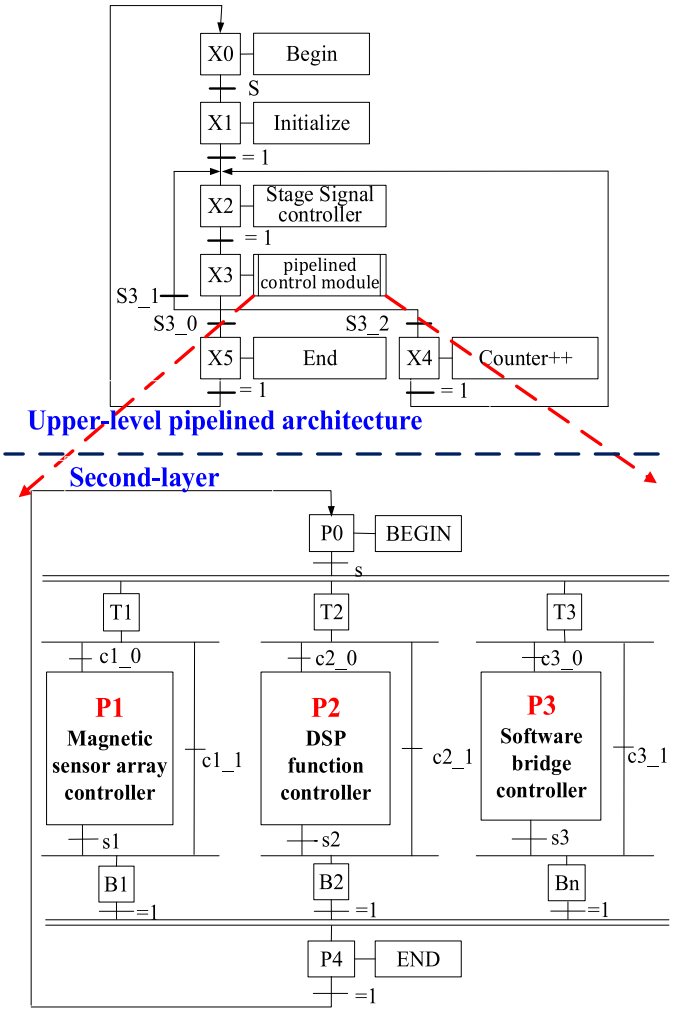


Fig. 7. Overall architecture of the pipelined parallel controller module.

that guarantees that the MFI system performs optimally and delivers accurate results.

III. Discrete-Event Modeling and High-Level Synthesis

In this section, we further explain the architecture of the three main functional controller modules, which are synthesized into a pipelined parallel controller by using the generic pipelining model proposed in [18]. We also describe the operational steps of the pipelined parallel controller.

Fig. 7 presents the overall architecture of the pipelined system. The two key top-level modules are the stage signal controller (X2) and the pipe controller and pipelined control module (X3). The X2 controller generates control signals (see Fig. 8) and conditionally controls the pipelined control module (X3) for each step (e.g., P1, P2, . . . , Pn). The X3 controller is the second-layer building block of the main module.

The X3 submodule's actions are based on the signals generated by the stage signal controller (X2).

Within the submodule, steps T1, T2, . . . , Tn, and B1, B2, . . . , Bn are idle steps that do not control any combinational logic elements or other submodules. They primarily stabilize the transmission of control signals. The pipelined

cycle	Stage 1	Stage 2	Stage 3	.....	Stage n
1	1				
2	1	1			
3	1	1	1		
.....					
n-1	1	1	1	1... 1	
n	1	1	1	1... 1	1
.....					
k (final data)	1	1	1	1... 1	1
k+1		1	1	1... 1	1
k+2			1	1... 1	1
.....					
k+n-1					1

Fig. 8. Table of the stage control signal for an n-stages pipelined system.

parallel controller was designed in accordance with modular construction principles; the operation of each system can be divided into stages, and each stage represents the P1, P2, . . . , Pn steps of each pipelined control module (X3). This method enables the system's pipelined module architecture to be rapidly established.

Depending on the complexity of the system, designers might build multiple pipelined submodules at the lowest level, with each submodule corresponding to one of the P1, P2, . . . , Pn steps of each pipelined control module (X3).

When the pipelined architecture module transitions to the pipelined control module, step P0 immediately becomes idle, and steps T1, T2, . . . , Tn become active. The control signals generated by the stage signal controller trigger the conditions c1_0, c1_1, c2_0, c2_1, . . . , cn_0, cn_1, which, in turn, control the activity of steps P1, P2, . . . , Pn. During this time, steps T1, T2, . . . , Tn are idle.

The actions of steps P1, P2, . . . , Pn trigger combinational logic elements or other modules. When these elements or modules complete their computations, they pass a completion signal to the transition conditions s1, s2, . . . , sn. The steps then transition to B1, B2, . . . , Bn while the modules wait for other elements or modules to complete their tasks. At this time, steps P1, P2, . . . , Pn are idle but step P4 is active, indicating that the pipelined control module has completed its computation.

The state then transitions to the upper-level pipelined architecture module. In the next cycle, step P4 becomes idle and the module immediately returns to the initial state P0 while it waits for the next signal to trigger the pipelined control module.

These submodules are integrated into the overall pipelined architecture module (see Fig. 7); thus, modules for the multilayered pipelined parallel controller architecture are rapidly established.

The control mechanism for generating signals in the stage signal controller is such that, in the first cycle, the first stage is active, and the other stages are idle. In the second cycle, both the first and second stages are active, and the others are idle. This pattern continues until the nth stage, at which the data for the first cycle has been correctly computed and output by all n processes.

Authorized licensed use limited to: National Central University. Downloaded on July 02,2024 at 07:18:47 UTC from IEEE Xplore. Restrictions apply.

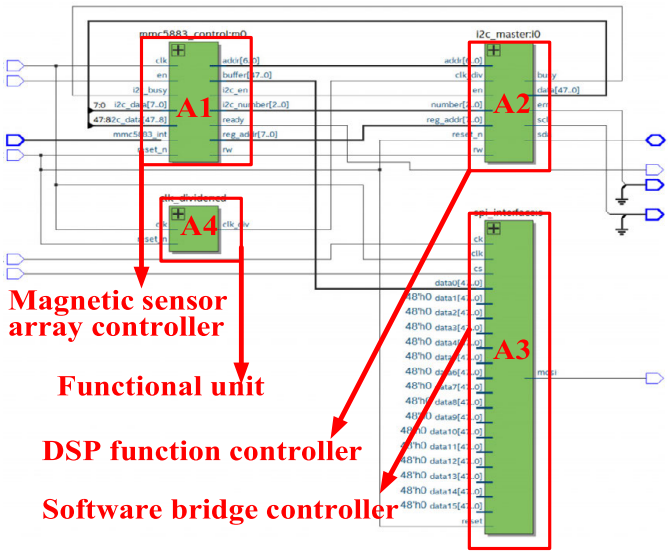


Fig. 9. VLSI hardware circuit of the child controller.

As shown in Fig. 8, for k data and n stages, a total of $k+n-1$ cycles are required for all data to be fully processed.

The actions of steps P1, P2, and P3 in the pipelined control module (X3) are determined by the signals generated by the stage signal controller.

Fig. 9 presents the entire VLSI hardware circuit of the function modules for the parallel controller, as created in accordance with our design methodology.

By adopting the hierarchical modular design and automatic hardware synthesis detailed in Section II to design all of the intelligent functional modules, we achieved complete integration of the pipelined parallel controller into the hardware architecture.

In addition, to confirm that all function modules were successfully mapped to the VLSI hardware circuit after the automatic hardware synthesis process, we used the register transfer level viewer to inspect and analyze the synthesized parallel controller's hardware circuit. As illustrated in Fig. 9, the parallel controller circuit comprises the magnetic sensor array controller (A1) module, the DSP function controller (A2) module, the software bridge controller (A3) module, and the function unit (A4) module.

The system modeling and hardware synthesis methodology outlined in this article enables the comprehensive integration of multiple functional modules, meeting the interconnection, intercommunication, interaction, and interoperation requirements of a complex system design. This ensures the seamless operation and coordination of the MFI system.

IV. Implementation

A. System Integration and Verification

The hardware architecture used to implement the MFI system is displayed in Fig. 10; it has three layers: the perception layer, the control layer, and the software layer.

A prototype of the MFI system is presented in Fig. 11. The perception layer comprised 16 AMR sensors each, including an MMC5883MA chip. These 16 AMR sensors were arranged

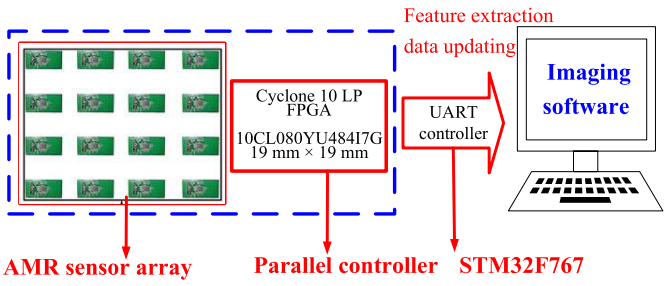


Fig. 10. Hardware architecture of the MFI system.

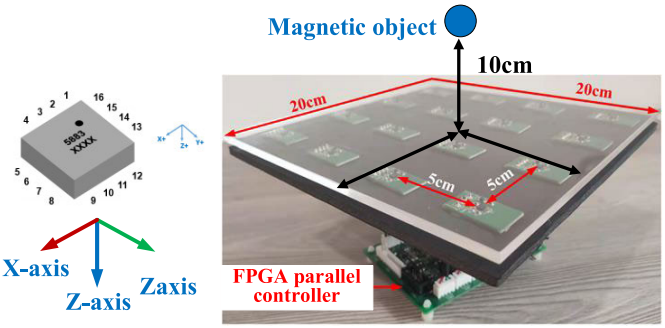


Fig. 11. Prototype MFI system.

in a 4 × 4 grid and affixed to the testing platform. The length and width of the platform were both 20 cm. Each AMR sensor was positioned 5 cm from its neighbors, ensuring high sensitivity.

The left side of Fig. 11 indicates that the x-, y-, and z-axes of the platform were aligned with a reference direction [28].

The control layer employed an FPGA, the Intel 10CL080YU484I7G, for implementing the parallel controller. The FPGA parallel controller was responsible for DSP, controlling the AMR sensor nodes through I^2C, and communicating with the software through an SPI and a UART controller. UART controller (STM32F767ZI) is responsible for feature data packaging and transmission.

The software-layer imaging program was constructed using the Matplotlib plotting library. Its primary function was to transform real-time output data from the platform into a dynamic visualization on an interface.

After the initialization of the system by the parallel controller, parallel computing was begun through clock synchronization. During a given clock period, the perception layer acquired the magnetic field components from 16 AMR sensors in parallel, and the control layer parallel-processed 16 sets of magnetic field components and performed preprocessing, multichannel data fusion, and feature extraction calculations; finally, the control layer transmitted the feature extraction data. The platform data could then be input into the integrated imaging software to realize the MFI system for NDT applications.

B. Function Verification of the FPGA Parallel Controller

We validated three crucial functions of the MFI system: parallel acquisition of magnetic field components from the 16 AMR sensors, parallel data processing, and intermodule parallel transmission.

Authorized licensed use limited to: National Central University. Downloaded on July 02,2024 at 07:18:47 UTC from IEEE Xplore. Restrictions apply.

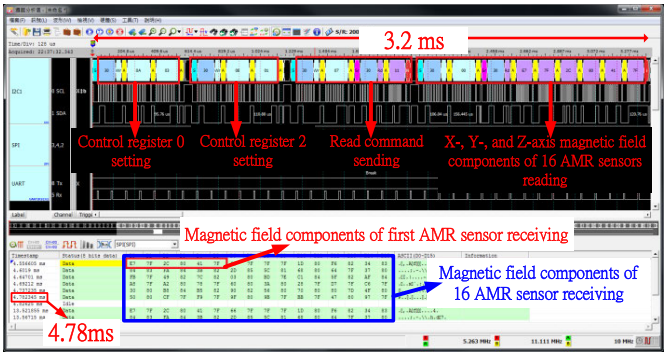


Fig. 12. Data transmission of the magnetic sensor array, visualized using a logic analyzer (TL2236).

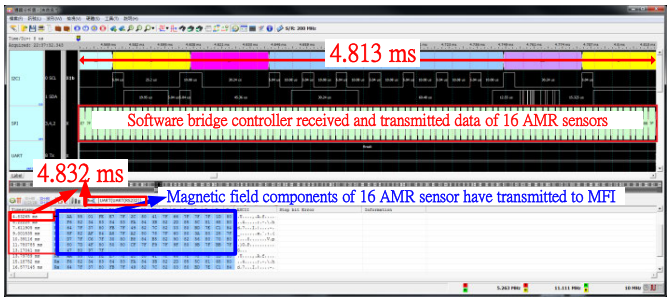


Fig. 13. Data reception by the software system, visualized using a logic analyzer (TL2236).

Figs. 12 and 13 present the transmission status and utilization, respectively, of the three communication interfaces: I^2C, SPI, and UART. The I^2C interface handled the parallel acquisition of data from the 16 AMR sensors by the main controller, and feature data were output from the main controller over the SPI. The main controller and the imaging software communicated over UART.

Fig. 12 reveals that during a 3.2-ms time interval (top red arrow), the system successfully acquired data from the 16 AMR sensors in parallel. The red box at the bottom left of Fig. 12 indicates the first set of feature data received by the software bridging controller module through the SPI. All feature data were received by the module within 4.78 ms.

Similarly, Fig. 13 shows that the UART controller completed the transmission of the first set of feature data to the imaging software within 4.832 ms.

We also confirmed that the system's DSP module provided the correct results and that the DSP algorithm was feasible. The system platform acquired the magnetic components of the object 300 consecutive times while simultaneously performing magnetic signal processing. In the test, the processed magnetic field signals were the raw magnetic components measured in the unit of the nanotesla (nT). We visualized the data to facilitate observations of the results.

The results are depicted in Fig. 14. The red, green, and blue lines indicate the results for the x-, y-, and z-axes, respectively. Fig. 14(a) presents the x-axis components before execution of the DSP algorithm; the range of the components was approximately 3000 nT. After DSP processing, this range was 7 nT [see Fig. 14(b)]. Similarly, DSP processing reduced the range of the y- and z-axis components from approximately 3500 to 5 nT [see Fig. 14(d) and (e)].

C. Dynamic Visualization

The imaging software was intended to dynamically display the data sensed by the platform in real time. This function was validated for the x, y, and z directions. A magnetic object was moved closer to the platform, resulting in a change in the measured magnetic field components. The object was then returned to its original position, and the magnetic field component returned to approximately its initial state. The measurement results are presented in Fig. 15. For a magnetic object moved 10 cm in the x-direction [see Fig. 15(a)], the imaging software revealed that the x-axis magnetic component changed by approximately 300 nT, from 32 650 to 32 350 nT. Similarly, moving the magnetic object 10 cm in the y and z directions, respectively, resulted in changes in the corresponding components of 600 and 500 nT; the components changed from 32 800 to 32 200 and from 32 700 to 32 200 nT, respectively [see Fig. 15(b) and (c)].

When the magnetic object was closest to the platform, the dynamic visual display exhibited a small offset. This can be observed in the z-axis measurement in Fig. 15(c). The offset was attributed to the vertical dynamic visual real-time verification as the magnetic object was moved from the top to the bottom and interacted with the platform. Because the validation requires precise positioning of the object directly above the platform at a distance of 10 cm, slight movements of the object during the initial validation can lead to small offsets of the type seen in Fig. 15(c); however, these small offsets also demonstrate the high sensitivity and accuracy of the designed MFI system.

The dynamic imaging was presented through a developed graphical user interface (GUI). The GUI resembled a chessboard, comprising 4 × 4 colored squares indicating the strength of the measured magnetic components; the vertical axis presents a legend (see Fig. 16). A total of eight magnetic objects were used as targets. The magnetic objects were positioned 10 cm away from the platform and uniformly moved toward it. Fig. 16(a) presents the system at initialization with no sensing targets on the platform; the color distribution is the default distribution. Fig. 16(b) presents the dynamic imaging graph when multiple targets were present on the platform, and Fig. 16(c) displays the results for the targets in different positions.

In Fig. 16(a)–(c), the variation in the magnetic field components decreases from 56 500–57 000 nT to less than 55 000 nT. This is equivalent to a recognition accuracy of 0.5 G.

D. Discussion

Table I presents a comparison of the proposed system with other systems reported in the literature. The innovations of the proposed technologies can be summarized as follows.

1) Real Time: For most state-of-the-art technologies, the execution time and the read and write times have not been clearly or completely reported. For example, [1], [2], [3], [4], [5], [6], [7] only briefly examined the execution time and

Authorized licensed use limited to: National Central University. Downloaded on July 02,2024 at 07:18:47 UTC from IEEE Xplore. Restrictions apply.

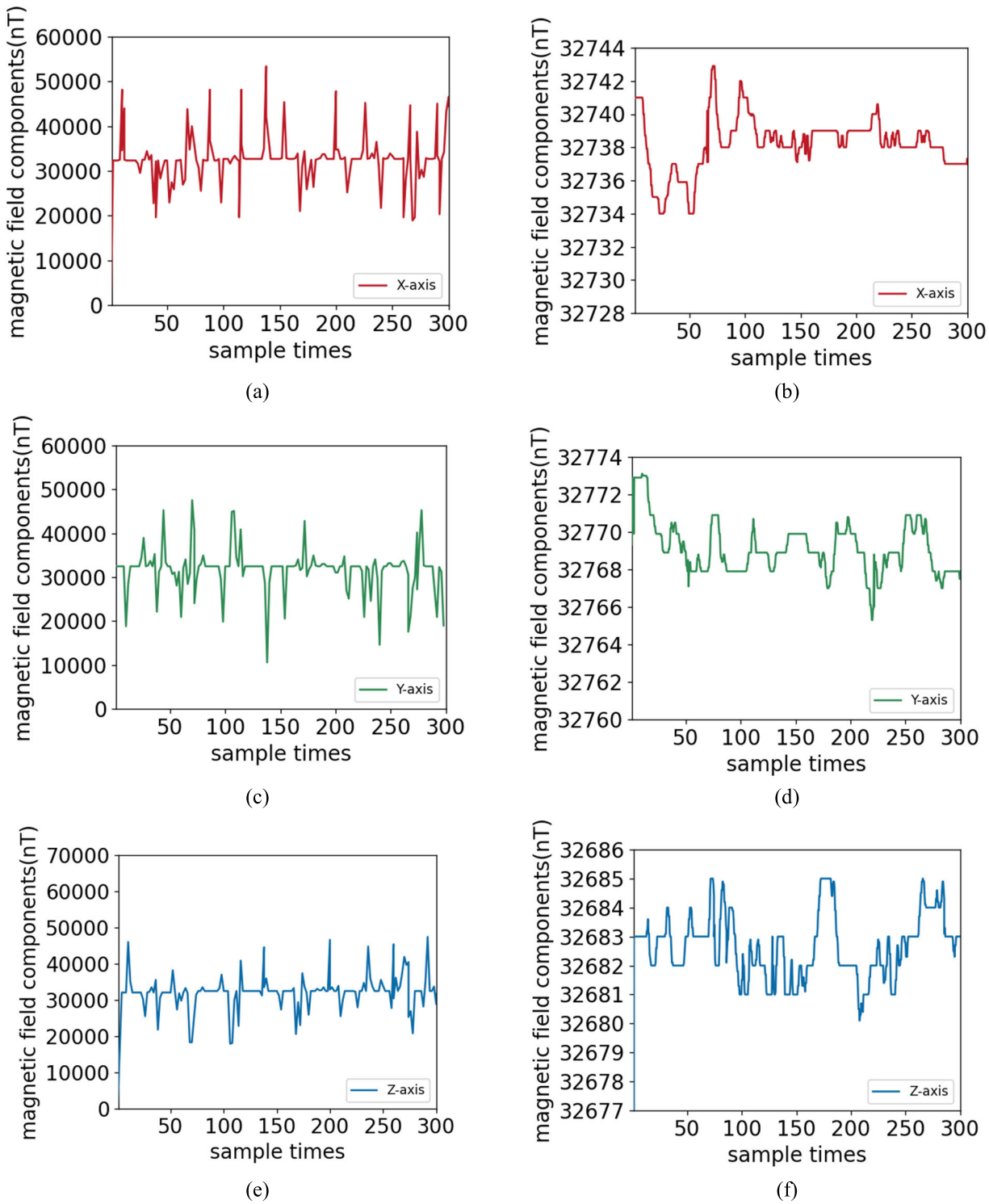


Fig. 14. Measured magnetic field data before and after DSP with the FPGA parallel controller: x-axis components (a) before and (b) after processing; y-axis components (c) before and (d) after processing; and z-axis components (e) before and (f) after processing.

sampling speed relevant to DAQ systems. In [8], the execution time was claimed to be 1 s; this was, however, obtained for only two TMR sensors, which is considerably fewer than are required for real-time measurements. In [14] and [15], moreover, the reported execution time (the time until the reception of responses from the 16 AMR sensors through the MCU) was 40 ms. By contrast, the execution time from the 16 AMR sensors to the software system through the high-speed FPGA parallel controller in our design was only 4 ms (see Section IV-B). The proposed solution thus performs much better than the typical solutions and could achieve the real-time measurement that is required for industrial applications.

2) Reliability: Sensor array systems with coils have various physical limitations [4], [17]. Coil-based sensor systems have

Authorized licensed use limited to: National Central University. Downloaded on July 02,2024 at 07:18:47 UTC from IEEE Xplore. Restrictions apply.

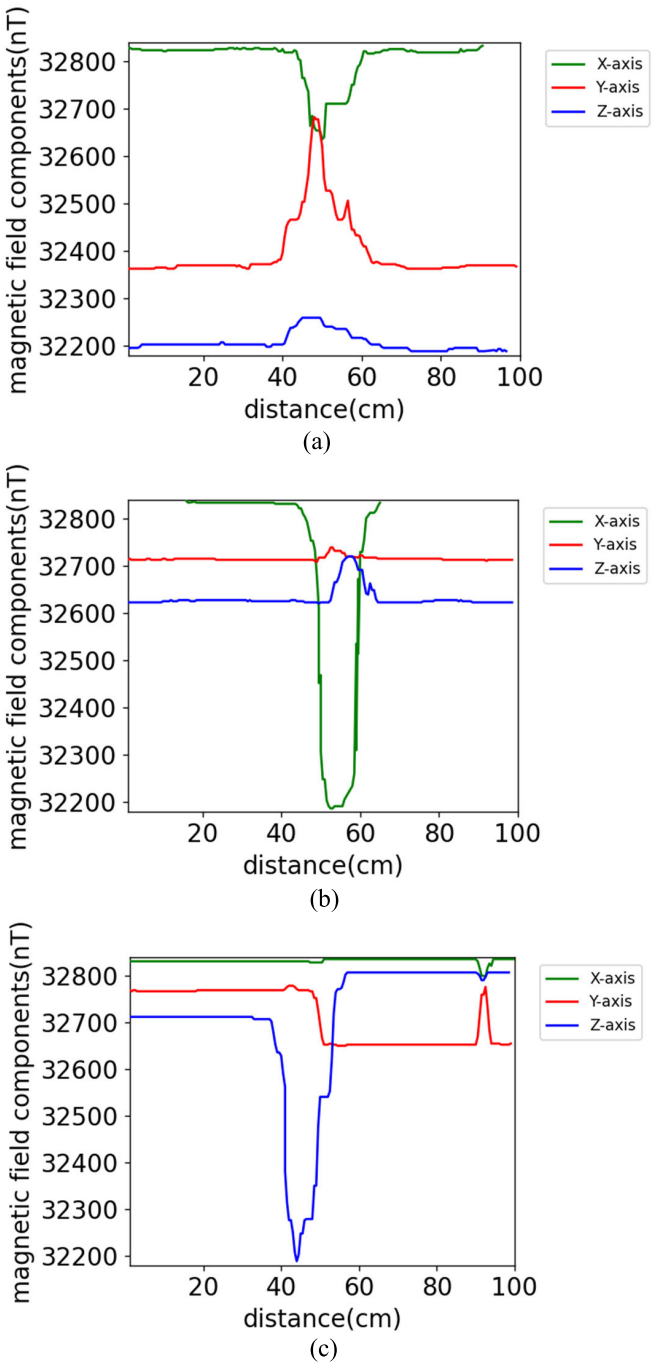


Fig. 15. Dynamic visualization of directional measurements with a magnetic object: (a) x-, (b) y-, and (c) z-axis measurements.

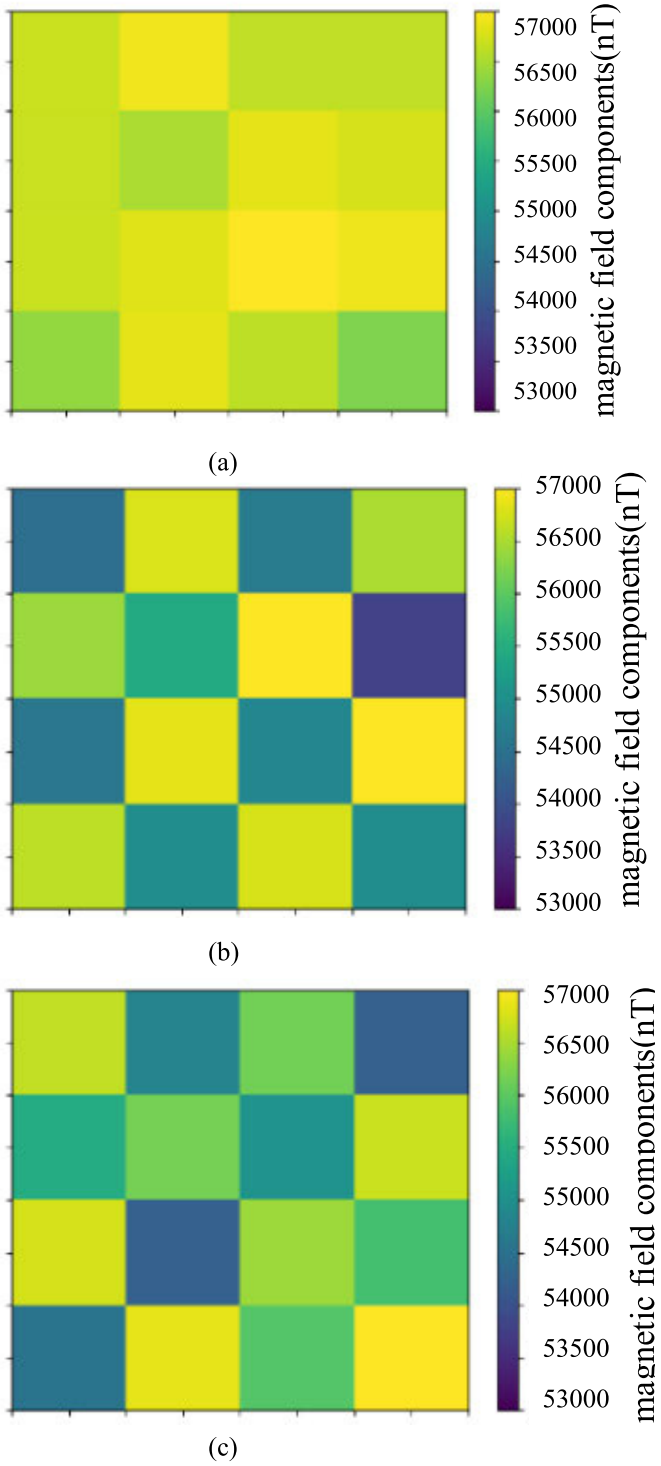


Fig. 16. MFI verification. (a) Pesents the system at initialization with no sensing targets on the platform; the color distribution is the default distribution. (b) Presents the dynamic imaging graph when multiple targets were present on the platform. (c) Displays the results for the targets in different positions.

a large volume, and the diameter of these coils limits the resolution of a sensor array. Additionally, the coupling between coil sensors affects the detection accuracy. To overcome these drawbacks, MEMS fabrication was used to produce AMR sensors in a 4 × 4 array in the proposed system, and this setup reduced mutual inductance between coils. By using a reconfigurable FPGA for high-speed parallel computing, we enhanced the efficiency of transmitting detected data and ensured the detection system's reliability. We, furthermore, adopted the Matplotlib plotting library to develop software algorithms for visualizing the detected data.

3) Stability: Our survey revealed that most state-of-the-art technologies do not have guaranteed stability. To achieve high reliability and stability, we proposed an MFI system with an FPGA parallel controller and a high-sensitivity AMR sensor array. The function controllers of the parallel algorithm are implemented as fully hardware-accelerated modules with pipelined architecture in the FPGA parallel controller, improv-

Authorized licensed use limited to: National Central University. Downloaded on July 02,2024 at 07:18:47 UTC from IEEE Xplore. Restrictions apply.

TABLE I
COMPARATIVE ANALYSIS WITH STATE-OF-THE-ART TECHNOLOGIES

	Array type	Number	Method.	Imaging
[1]	Flexible array probe	16 FPCB-coil	ECT	MATLAB.
[2]	Flexible array probe	16 TMR	ECT	MATLAB.
[3]	Differential coil sensors	A pair of coils	ECT	MATLAB.
[4]	Flexible array probe	64 TMR	ECT	MATLAB.
[5]	Flexible array probe	64 TMR	ECT	COMSOL Multiphysics
[6]	Fabricated on PCB	180 TMR	ECT	N/A
[7]	FPCB-coil	24 excitation coils 12 pickup coils	ECT	FEM
[12]	AMR sensor	1 excitation coil 1 AMR	ECT	COMSOL Multiphysics
[8]	Sensor probe	Coil sensors 2 TMR	MFL	N/A
[9]	Sensor probe	6 AMR	MFL	N/A
[10]	Flexible sensor array	6 GMR	MFL	FEM, ANSYS
[11]	Flexible sensor array	6 GMR	MFL	FEM, ANSYS
[13]	Planar PCB-coil	16 AMR	2-D current distribution	N/A
[14] [15]	Sensor array	16 AMR	Magnetic field component	MATLAB
Proposed.	Sensor array	16 AMR	Magnetic field component	Matplotlib

ing the performance compared with that of an MCU. The experimental results revealed that the proposed system is sensitive to magnetic objects in any orientation, indicating the system's stability and effectiveness; moreover, our solution does not require multiplexing of excitation coils, reducing its cost and noise and ensuring a high detection speed.

We conducted a comprehensive survey of state-of-the-art technologies for magnetic imaging systems based on 16-element arrays of MR sensors [1], [2], [13], [14], [15]. Magnetic source imaging technologies can be categorized as active and passive detection technologies. Active technologies use active coil sensors [1], [2] to generate a magnetic field for detecting anomalies in the three-axis magnetic field components of underground or internal metal structures. Passive technologies employ passive magnetic field sensors [13], [14], [15] to measure subtle three-axis magnetic field components in the environment.

Despite the numerous advantages of the active electromagnetic detection systems presented in [1] and [2], one paper noted that coil sensors might be ineffective for precise localization [15]. Additionally, coil detection systems require complex laboratory circuit designs and support from various equipment, instruments, and devices, making them impractical for real-world applications. Various studies [13], [14], and [15] have used MCUs as the control core for a magnetic field sensor array system; however, as the number of sensors was increased, the MCU's performance was found to become inadequate for simultaneously processing data from multiple sensors. The proposed system with an FPGA parallel controller greatly outperforms the MCU-based systems and the industrial real-time requirement.

V. CONCLUSION

To address the drawbacks of typical coil detection systems and overcome the limited hardware resources of MCUs for magnetic field sensor array systems, an MFI system based on a 4 × 4 AMR sensor array architecture was proposed in this study. The system has high precision, sensitivity, reliability, and stability for magnetic field sensing. In the control layer, the main controller is designed to have pipelined parallelization architecture, and the hardware circuit includes multiple intelligent functional modules. The proposed system can effectively acquire magnetic field components from 16 AMR sensors in parallel and perform parallel data processing and parallel intermodule data transmission within 4 ms. Additionally, the system control unit does not require an operating system, complex circuit design, or additional equipment. The imaging software in the software layer was developed using open-source libraries to reduce costs, and it enables real-time dynamic visualization of the sensed information. The proposed system is expected to be used as a solution for various NDT applications, such as foreign object detection and field interference mapping for mobile devices.

ACKNOWLEDGMENT

The authors would like to thank the anonymous referees and the Editor for their valuable opinions.

REFERENCES

[1] C. Ye, N. Zhang, L. Peng, and Y. Tao, "Flexible array probe with in-plane differential multichannels for inspection of microdefects on curved surface," *IEEE Trans. Ind. Electron.*, vol. 69, no. 1, pp. 900–910, Jan. 2022.

[2] N. Zhang, L. Peng, Y. He, and C. Ye, "Flexible probe with array tunneling magnetoresistance sensors for curved structure inspection," *IEEE Trans. Instrum. Meas.*, vol. 71, pp. 1–9, 2022.

[3] N. Zhang, L. Peng, X. Tao, and C. Ye, "Flexible ECT probe with front-end differential setting for inspection of curved CFRP structures," *Compos. B, Eng.*, vol. 227, Dec. 2021, Art. no. 109404.

[4] N. Zhang, C. Ye, L. Peng, and Y. Tao, "Eddy current probe with three-phase excitation and integrated array tunnel magnetoresistance sensors," *IEEE Trans. Ind. Electron.*, vol. 68, no. 6, pp. 5325–5336, Jun. 2021.

[5] L. Peng, N. Zhang, Y. Tao, and C. Ye, "Fastener tilt assessment based on magnetic field image obtained with array tunnel magnetoresistance sensors," *IEEE Trans. Instrum. Meas.*, vol. 70, pp. 1–9, 2021.

[6] C. Ye, Y. Wang, and Y. Tao, "High-density large-scale TMR sensor array for magnetic field imaging," *IEEE Trans. Instrum. Meas.*, vol. 68, no. 7, pp. 2594–2601, Jul. 2019.

[7] N. Zhang, C. Ye, L. Peng, and Y. Tao, "Novel array eddy current sensor with three-phase excitation," *IEEE Sensors J.*, vol. 19, no. 18, pp. 7896–7905, Sep. 2019.

[8] M. Hayashi, T. Kawakami, T. Saito, K. Sakai, T. Kiwa, and K. Tsukada, "Imaging of defect signal of reinforcing steel bar at high lift-off using a magnetic sensor array by unsaturated AC magnetic flux leakage testing," *IEEE Trans. Magn.*, vol. 57, no. 2, pp. 1–4, Feb. 2021.

[9] M. Hayashi et al., "Crack detection for welded joint with surface coating using unsaturated AC magnetic flux leakage," *IEEE Trans. Magn.*, vol. 58, no. 8, pp. 1–5, Aug. 2022.

[10] M. Durai, P. Chi-Chuan, C.-W. Lan, and H. Chang, "Analysis of leakage in a sustainable water pipeline based on a magnetic flux leakage technique," *Sustainability*, vol. 14, no. 19, p. 11853, Sep. 2022.

[11] M. Durai, C.-W. Lan, and H. Chang, "In-line detection of defects in steel pipes using flexible GMR sensor array," *J. King Saud Univ.-Sci.*, vol. 34, no. 2, Feb. 2022, Art. no. 101761.

Authorized licensed use limited to: National Central University. Downloaded on July 02,2024 at 07:18:47 UTC from IEEE Xplore. Restrictions apply.

[12] C.-Y. Lin, Y.-C. Wu, and M. Teng, "Development of a magnetic/eddy-current sensing system for simultaneous estimation of electrical conductivity and thickness in non-ferrous metal plates," *IEEE/ASME Trans. Mechatronics*, vol. 28, no. 1, pp. 360–371, Feb. 2023.

[13] G.-W. Huang and J.-T. Jeng, "Implementation of 16-channel AMR sensor array for quantitative mapping of two-dimension current distribution," *IEEE Trans. Magn.*, vol. 54, no. 11, pp. 1–5, Nov. 2018.

[14] D. Rahmawati, D. Danudirdjo, and A. B. Suksmono, "Magnetic imaging system based on HMC5883L sensor array," in *Proc. 5th Int. Conf. Instrum., Commun., Inf. Technol., Biomed. Eng. (ICICI-BME)*, Nov. 2017, pp. 1–5.

[15] A. B. Suksmono, D. Danudirdjo, A. D. Setiawan, D. Rahmawati, and R. P. Prastio, "A magnetic field camera for real-time subsurface imaging applications," *Appl. Sci.*, vol. 11, no. 8, p. 3302, Apr. 2021.

[16] *Magnetic Sensors: TDK Reports Preliminary Study Results for Real-Time Monitoring of Cardiac Activity Using Prototype MR Sensors*. Accessed: May 1, 2023. [Online]. Available: https://www.tdk.com/en/news_center/press/20190313_01.html

[17] Z. Mao, W. Zhai, Y. Shen, S. Zhao, and J. Gao, "Advanced metal detection system based on TMR sensor array," *J. Magn. Magn. Mater.*, vol. 543, Feb. 2022, Art. no. 168601.

[18] C.-H. Chen, L. Luoh, and M.-H. Guo, "A new design and implementation of hardware accelerator for line detection," *Microprocessors Microsystems*, vol. 61, pp. 179–197, Sep. 2018.

[19] C.-H. Chen, M.-Y. Lin, and W.-H. Lin, "Designing and implementing a lightweight WSN MAC protocol for smart home networking applications," *J. Circuits, Syst. Comput.*, vol. 26, no. 3, Mar. 2017, Art. no. 1750043.

[20] C.-H. Chen, M.-Y. Lin, and X.-C. Guo, "High-level modeling and synthesis of smart sensor networks for industrial Internet of Things," *Comput. Electr. Eng.*, vol. 61, pp. 48–66, Jul. 2017.

[21] C.-H. Chen, M.-Y. Lin, and X.-C. Guo, "High-performance fieldbus application-specific integrated circuit design for industrial smart sensor networks," *J. Supercomput.*, vol. 74, no. 9, pp. 4451–4469, Sep. 2018.

[22] C.-H. Chen, M.-Y. Lin, and C.-C. Liu, "Edge computing gateway of the industrial Internet of Things using multiple collaborative microcontrollers," *IEEE Netw.*, vol. 32, no. 1, pp. 24–32, Jan. 2018.

[23] C.-H. Chen, M.-Y. Lin, Y.-C. Shih, and C.-C. Chen, "High-precision time synchronization chip design for industrial sensor and actuator network," *Microprocessors Microsyst.*, vol. 91, Jun. 2022, Art. no. 104507.

[24] C.-H. Chen, M.-Y. Lin, and W.-P. Tew, "Wireless fieldbus networking with precision time synchronization for a low-power WSAN," *Microprocessors Microsystems*, vol. 90, Apr. 2022, Art. no. 104509.

[25] M.-Y. Lin, C.-H. Chen, S.-C. Chen, and C.-T. Liu, "Self-adaptive image codec for intelligent vision sensor networks," *Int. J. Inf. Technol.*, vol. 14, no. 5, pp. 2533–2540, Aug. 2022.

[26] M.-Y. Lin, C.-H. Chen, Z.-B. Dong, and C.-C. Chen, "Gigabit modbus user datagram protocol fieldbus network integrated with industrial vision communication," *Microprocessors Microsystems*, vol. 94, Oct. 2022, Art. no. 104682.

[27] M.-Y. Lin, S.-H. Hsieh, and C.-H. Chen, "Reconfigurable hardware accelerator of morphological image processor," in *Proc. IEEE 3rd Int. Conf. Electron. Commun., Internet Things Big Data (ICEIB)*, Apr. 2023, pp. 348–351.

[28] MEMSIC, Inc. *MMC5883MA*. Accessed: May 1, 2023. [Online]. Available: https:/www.memsic.com/

[29] Honeywell. *HMC5883L*. Accessed: May 1, 2023. [Online]. Available: https:/www.magneticsensors.com/



Ming-Yi Lin received the master's degree from Yuan Ze University, Taoyuan, Taiwan, in 2011, and the Ph.D. degree in computer science from National Central University, Taoyuan, in 2016.

He was an Assistant Professor with the Department of Computer Science and Information Engineering, Chinese Culture University, Taipei, Taiwan, in 2021. He is currently an Assistant Professor with the Department of Computer Science and Engineering, Yuan Ze University. His research interests include embedded systems, smart sensor networks, and AIoT.



Sheng-Hsien Hsieh received the Ph.D. degree in electrical engineering from I-Shou University, Kaohsiung, Taiwan, in 2010.

He is currently serving as an Assistant Professor in the program of artificial intelligence and mechatronics with the National Pingtung University of Science and Technology, Pingtung, Taiwan. His research interests include computer vision, artificial intelligence, and embedded system design.



Ching-Han Chen received the Ph.D. degree from Franche-Comte University, Besançon, France, in 1995.

He was an Associate Professor with the Department of Electrical Engineering, I-Shou University, Kaohsiung, Taiwan, in 1995. He is currently a Professor with the Department of Computer Science and Information Engineering, National Central University, Taoyuan, Taiwan. His research interests include embedded system design, AIoT, and robotics.



Chun-Hung Lin received the master's degree in communication engineering from National Central University, Taoyuan, Taiwan, in 2021.

He is currently a Hardware Engineer with International Games System Company Ltd., New Taipei City, Taiwan. His research interests include embedded systems, mechatronics, and the Internet of Things.

Authorized licensed use limited to: National Central University. Downloaded on July 02,2024 at 07:18:47 UTC from IEEE Xplore. Restrictions apply.